Chinese Chemical Letters 37 (2026) 110729

Contents lists available at ScienceDirect

Chinese Chemical Letters

journal homepage: www.elsevier.com/locate/cclet

Effect of crystal morphology of nickel-rich cathode materials on electrochemical stability and ion transport kinetics of sulfide-based all-solid-state batteries

Shanyan Huang[a], Bi Luo[b,*], Zixun Zhang[b], Qi Wang[b], Guihui Yu[b], Xudong Bu[c], Zheng Huang[d], Xiaowei Wang[b], Wei-Li Song[a,*], Jiafeng Zhang[b,*], Shuqiang Jiao[c,d]

[a] Institute of Advanced Structure Technology, Beijing Institute of Technology, Beijing 100081, China
[b] National Engineering Laboratory for High Efficiency Recovery of Refractory Nonferrous Metals, School of Metallurgy and Environment, Central South University, Changsha 410083, China
[c] State Key Laboratory of Advanced Processing and Recycling of Non-ferrous Metal, Lanzhou University of Technology, Lanzhou 730050, China
[d] State Key Laboratory of Advanced Metallurgy, University of Science and Technology Beijing, Beijing 100083, China

ARTICLE INFO

Article history:
Received 13 September 2024
Revised 28 November 2024
Accepted 5 December 2024
Available online 6 December 2024

Keywords:
Nickel-rich cathode
Sulfide-based solid electrolytes
Single-crystalline materials
Ion transport kinetics
Solid-state batteries

ABSTRACT

Nickel-rich layered oxides are considered highly promising cathode materials for all-solid-state batteries (ASSBs) due to their high theoretical specific capacity and energy density. In this study, a comparison between polycrystalline and single-crystalline cathode materials was conducted. It was found that, during the charging process, ion transport at the interface of polycrystalline cathodes is significantly influenced by phase transitions and side reactions with the electrolyte, resulting in an irreversible increase in impedance after cycling. Furthermore, the structural stability of the cathode material affects internal ion diffusion kinetics, thereby influencing its electrochemical performance. Unlike single-crystalline materials, ion migration in polycrystalline materials must traverse anisotropic grain boundaries, which, due to anisotropic lattice contraction, evolve into intergranular cracks, leading to reduced ion diffusion kinetics and degraded electrochemical performance. In contrast, single-crystalline cathodes exhibit more stable interfacial resistance and uniform ion transport during charging, ensuring structural stability over long-term cycling. Consequently, at a 0.5 C rate, the single-crystalline cathode maintains a specific capacity of 143 mAh/g after 500 cycles, with a capacity retention of 89.2 %, while preserving its intact single-crystal morphology. This study provides valuable new insights into the localized lithium-ion transport behavior in single-crystalline and polycrystalline cathode materials for sulfide-based all-solid-state batteries.

© 2025 Published by Elsevier B.V. on behalf of Chinese Chemical Society and Institute of Materia Medica, Chinese Academy of Medical Sciences.

With the rapid development of renewable energy and new energy vehicles, the field of electrochemical energy storage devices has entered a period of high-speed growth [1–3]. However, the large-scale use of lithium-ion batteries is currently hindered by their insufficient energy density and inherent safety hazards, thereby limiting the further development and application of new energy vehicles [4–6]. All-solid-state batteries (ASSBs) based on inorganic solid electrolytes have garnered significant attention and research due to their high energy density and enhanced safety, being regarded as the most promising energy storage devices for the next generation [7–9]. Nevertheless, there are still challenges in the large-scale production and energy density enhancement of solid-state batteries, preventing their widespread application in new energy vehicles [10].

As the core component of solid-state batteries, the ionic conductivity and electrochemical/chemical stability of solid electrolytes have a profound impact on the cycle stability and energy density of these batteries [11]. Among various solid electrolyte materials, sulfide-based solid electrolytes have emerged as the current research focus due to their high ionic conductivity ($>10^{-3}$ S/cm), low grain boundary resistance [12]. Based on their chemical compositions, all known sulfide-based solid electrolytes can be classified into glassy sulfides [13,14], halogenated thiophosphates [15,16], thiophosphates [17], phosphorus-free sulfides [18]. However, despite their advantages, these sulfide-based electrolytes are not widely adopted in energy storage systems. Most of them, while possessing high ionic conductivity, cannot serve as direct replacements for their liquid counterparts due to their

* Corresponding authors.
E-mail addresses: biluo@xtu.edu.cn (B. Luo), weilis@bit.edu.cn (W.-L. Song), yjyzjf@csu.edu.cn (J. Zhang).

https://doi.org/10.1016/j.cclet.2024.110729
1001-8417/© 2025 Published by Elsevier B.V. on behalf of Chinese Chemical Society and Institute of Materia Medica, Chinese Academy of Medical Sciences.

non-competitive electrochemical performance, encompassing specific capacity, initial Coulombic efficiency, and capacity retention rate [19–21]. Moreover, numerous challenges persist, such as space charge layers, interfacial reactions, lithium dendrite growth, and chemical-mechanical failures [22–24].

As another crucial component in ASSBs, cathode materials are also vital to the performance of ASSBs [25]. Among various cathode materials, nickel-rich layered oxides are considered a promising option due to their high theoretical specific capacity and high energy density [26–28]. However, when sulfide-based solid electrolytes are combined with nickel-rich layered oxide cathodes to construct ASSBs, the high electrochemical potential of the cathode facilitates the easy transfer of Li^+ from the electrolyte side to the cathode side. For sulfide electrolytes with high ionic conductivity, the weaker intermolecular interactions lead to a rapid decrease in lithium concentration at the interface, resulting in the formation of a lithium-depleted layer [29]. Additionally, traditional polycrystalline nickel-rich layered oxides suffer from poor cycle life due to their fragile microstructures [30]. During cycling process, the polycrystalline primary particles undergo anisotropic volume changes, and significant anisotropic volume changes within secondary particles can lead to large stresses and grain boundaries, ultimately causing chemical-mechanical degradation [31–33]. Especially in ASSBs, the solid-solid contact between active particles and solid electrolyte particles limits ion transport at the solid-solid interface, exacerbating this structural degradation [34]. Recently, the application of single-crystalline cathode eliminates grain boundaries present in traditional heterogeneous polycrystals, significantly inhibiting the accumulation of stresses and strains caused by volume changes during (de)lithiation [35–37]. Although single-crystalline nickel-rich layered oxides have been reported as cathode materials for sulfide-based ASSBs, there is still a lack of comprehensive understanding of the advantages of single-crystalline cathodes in ASSBs [38–40]. Understanding of the ion transport kinetics of solid/solid interfaces between single-crystalline and polycrystalline cathode materials is important to address these interface issues in sulfide-based ASSBs.

In this study, we investigated the electrochemical performance and interfacial dynamics of polycrystalline (P-NCM83) and single-crystalline (S-NCM83) nickel-rich $LiNi_{0.83}Co_{0.12}Mn_{0.05}O_2$ cathodes in sulfide-based ASSBs. The results revealed that the ion transport at the interface of the polycrystalline cathode during charging is susceptible to phase transitions of the cathode and side reactions with the electrolyte, leading to an irreversible increase in impedance after cycling. Moreover, the grain boundaries in polycrystalline cathodes result in uneven charge distribution within secondary particles, limiting ion transport kinetics and causing uneven stress distribution within the secondary particles. During long-term cycling, the combination of increased interfacial resistance and the heterogeneous localized environment within the particles easily leads to the formation of intergranular cracks in polycrystalline cathodes, restricting solid-solid ion transport and causing performance degradation. In contrast, single-crystalline cathode materials exhibit more stable interfacial resistance and more uniform ion transport during charging, allowing for structural stability over long-term cycling. Compared to polycrystalline nickel-rich cathodes (P-NCM), the single-crystalline cathode electrode delivers a higher specific capacity of 143 mAh/g with a higher capacity retention of 89.2%, while maintaining an intact single-crystal morphology. This study deepens the understanding of the relationship between crystalline morphology and electrochemical stability and provides guidance for optimizing nickel-rich cathode materials for sulfide-based ASSBs.

Initially, the morphologies of P-NCM83 and S-NCM83 cathode materials were characterized by SEM. As depicted in Figs. 1a and b and Fig. S1a (Supporting information), P-NCM83 polycrystalline is

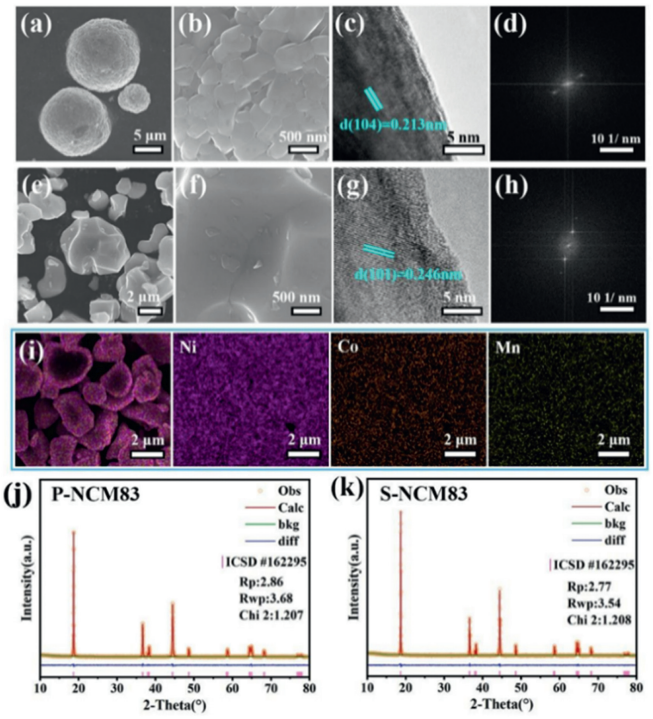


Fig. 1. (a, b) SEM images, (c) HRTEM image and (d) FFT results for P-NCM83. (e, f) SEM images, (g) HRTEM image, (h) FFT results and (i) element mappings for S-NCM83. Rietveld refinements of X-ray diffraction pattern for (j) P-NCM83 and (k) S-NCM83 cathode.

comprised of nano-sized primary particles to form spherical secondary particles with diameters ranging of 5–10 μm. The clear and uniform lattice spacings of 0.21 nm is observed in HRTEM image (Fig. 1c), which is consistent with the (104) plane in the layered structure, and can be further confirmed in the FFT pattern (Fig. 1d). In contrast, S-NCM83 single-crystalline particles exhibit smooth primary particles with particle sizes of approximately 2–5 μm (Figs. 1e and f, Fig. S1b in Supporting information). The distinct lattice spacings of 0.24 nm in the HRTEM image corresponds to the (101) plane in the layered structure (Figs. 1g and h). Moreover, elemental mapping images of P-NCM83 and S-NCM83 indicate a uniform distribution of Ni, Co, Mn, and other elements within the materials (Fig. 1i).

Furthermore, the XRD patterns and refinement results of P-NCM83 and S-NCM83 are presented in Figs. 1j and k, respectively. The pronounced splitting of the (006)/(102) peaks and the refined c/a values (Table S1) confirm that both P-NCM83 and S-NCM83 possess well-defined layered structures, belonging to the pure hexagonal α-$NaFeO_2$ structure within the *R-3m* space group [33]. Notably, both materials exhibit low Li/Ni cation mixing, contributing to their favorable kinetic properties. Additionally, XPS analysis was conducted to examine the chemical composition and elemental valence states of the materials. As shown in Fig. S2 (Supporting information), S-NCM83 exhibits less residual Li_2CO_3 on its surface compared to P-NCM83. By deconvoluting the Ni 2p3/2 peak into Ni^{2+} and Ni^{3+} components, the Ni^{3+} content in the materials can be analyzed. As illustrated in Fig. S2b (Supporting information), the Ni^{3+} content in P-NCM83 is approximately 77.8%, while that in S-NCM83 is around 81.6%. A higher Ni^{3+} content and lower Ni^{2+} content can reduce Li/Ni cation mixing, enhancing the structural stability of the material [41].

To evaluate the application potential of nickel-rich cathode materials in sulfide-based solid-state batteries, $Li_{5.5}PS_{4.5}Cl_{1.5}$ (LPSCl) electrolyte was employed as the solid-state electrolyte [42]. As

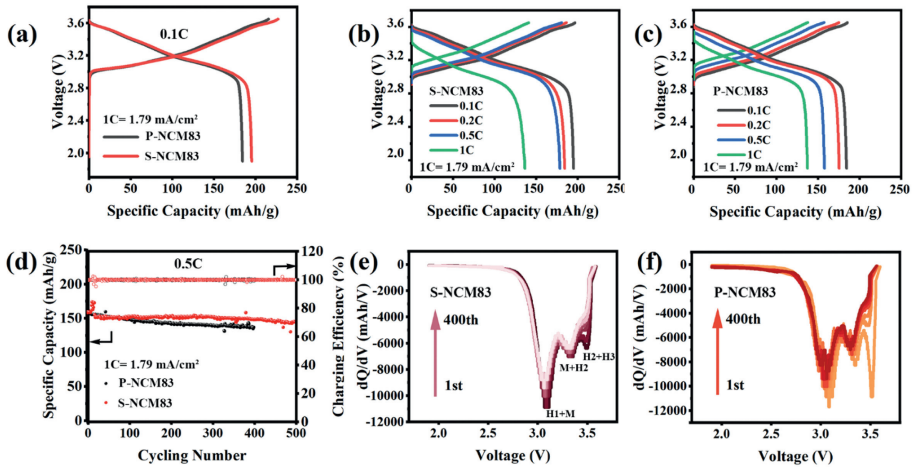


Fig. 2. (a) Charging-discharging curves of first cycle of NCM/LPSCl/Li-In cell at 0.1 C. Charging-discharging curves of NCM/LPSCl/ Li-In cell at different current density for (b) S-NCM83 and (c) S-NCM83 cathode. (d) Long cycling performance of NCM/LPSCl/Li-In. d*Q*/d*V* curves for (e) S-NCM83 and (f) S-NCM83 cathode.

shown in Fig. S3a (Supporting information), the LPSCl is composed of agglomerated particles and delivers a particle size of 20–40 μm. Additionally, the XRD pattern (Fig. S3b in Supporting information) shows that the LPSCl display a similar high cubic argyrodite-type crystallinity, matching well with the referenced Li_7PS_6 (PDF #34–0688). The Nyquist plots measured for the LPSCl electrolyte at room temperature are shown in Fig. S3c (Supporting information), with a calculated ionic conductivity of approximately 3.2×10^{-3} S/cm. To highlight the exceptional cycling stability of the S-NCM83 electrode in a sulfide-based ASSBs, all electrochemical experiments were conducted within the voltage range of 1.9–3.65 V at room temperature (25 °C). As shown in Fig. 2a, the P-NCM83 electrode exhibits initial charging and discharging capacities of 215.7 and 184.5 mAh/g, respectively, with an initial coulombic efficiency of 85.54 %. The S-NCM83 electrode possess initial charging and discharging capacities of 227.1 and 195.4 mAh/g, respectively, with an initial coulombic efficiency of 86.3 %.

To gain a deeper understanding of the electrochemical behavior of high-nickel cathode materials in sulfide-based ASSBs, the first-cycle d*Q*/d*V* profiles are presented in Fig. S4 (Supporting information). During charging, both P-NCM83 and S-NCM83 electrodes undergo phase transitions from the layered phase (H1) to the monoclinic phase (M) and two hexagonal phases (H2 and H3) [43]. Notably, the H2 → H3 phase transition is accompanied by an abrupt anisotropic lattice contraction, leading to internal microcracks and capacity fading [44]. In comparison, the H2–H3 transition is considerably suppressed in S-NCM83, which enable a more reversible phase transition process. After the first charge-discharge cycle, the rate performance of the batteries was further evaluated at 0.1, 0.2, 0.5, and 1 C. As depicted in Fig. 2b, the specific capacities of the S-NCM83 battery under these conditions are 195.25, 184.71, 178.89, and 136.69 mAh/g, respectively. In contrast, the specific capacities of the P-NCM83 battery are 184.35, 175.44, 157.68, and 137.27 mAh/g, respectively (Fig. 2c). Furthermore, long cycling stability tests were conducted at 0.5 C (Fig. 2d), where the P-NCM83 battery experiences significant capacity fluctuations after 400 cycles and delivers a capacity of 141 mAh/g with a capacity retention rate of 88.1 %. In contrast, the S-NCM83 battery retains a capacity of 143 mAh/g and a capacity retention rate of 89.2 % after 500 cycles, which exhibit improved electrochemical performance compared to those of previously reported NCM based electrodes (Table S2 in Supporting information). To better understand the phase transitions during long cycling process, the charge-discharge curves and d*Q*/d*V* profiles at various cycles are presented in Fig. S5 (Supporting information), Figs. 2e and f, respectively. Compared

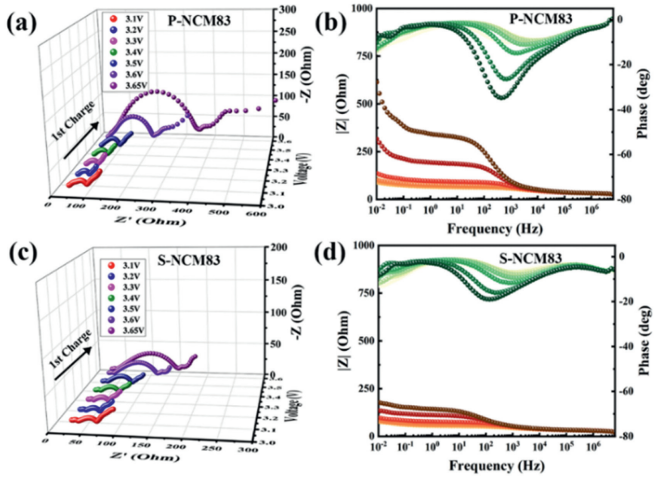


Fig. 3. *In-situ* impedance spectra of NCM/LPSCl/Li cell at 0.1 C. (a) Nyquist plots and (b) Bode plots of P-NCM83 cathode during the first charging process. (c) Nyquist plots and (d) Bode plots of S-NCM83 cathode during the first charging process.

to P-NCM83, the S-NCM83 battery exhibits less severe irreversible phase transitions during long-term cycling, enabling it to maintain a better structural integrity, which is consistent with the cyclic stability results.

To explore the changes in interfacial stability of P-NCM83 and S-NCM83 electrodes, the *in-situ* impedance spectroscopy was employed to analyze the interfacial impedance of the batteries during charging and discharging, which can provide valuable insights into how the electrode-electrolyte interface responds to the varying electrochemical conditions. To investigate the impedance variations, *in-situ* EIS spectra were measured at various voltages during the 0.1 C charging-discharging process.

Figs. 3a and b display the Nyquist plots and Bode plots, respectively, during the first charging process of P-NCM83 at 0.1 C. As shown in Fig. 3a, at the beginning of the first charging process, the slope in the low-frequency region of the Nyquist plots is relatively small, and as the charging potential increases, the low-frequency curve of the Nyquist plots gradually approaches a semicircle shape, accompanied by an increase in resistance. Correspondingly, the amplitude of the curve in the Bode plots also increases. When the open-circuit voltage (OCV) reaches 3.65 V, a regular semicircle appears in the low-frequency region of the Nyquist plots, indicating the maximum resistance, and the amplitude of the

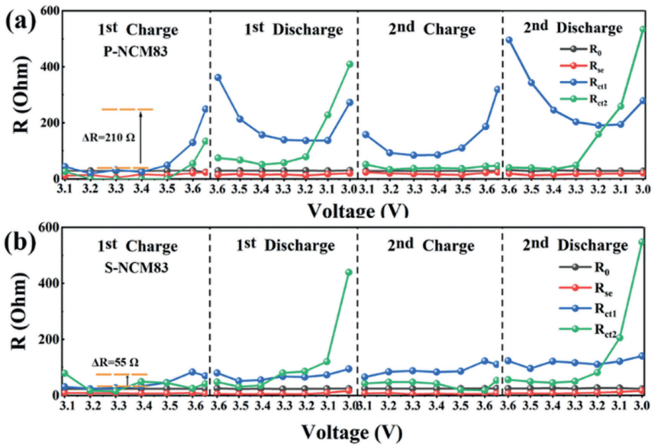


Fig. 4. Variation of the resistance values of (a) P-NCM83 and (b) S-NCM83 cathode during the first two cycles.

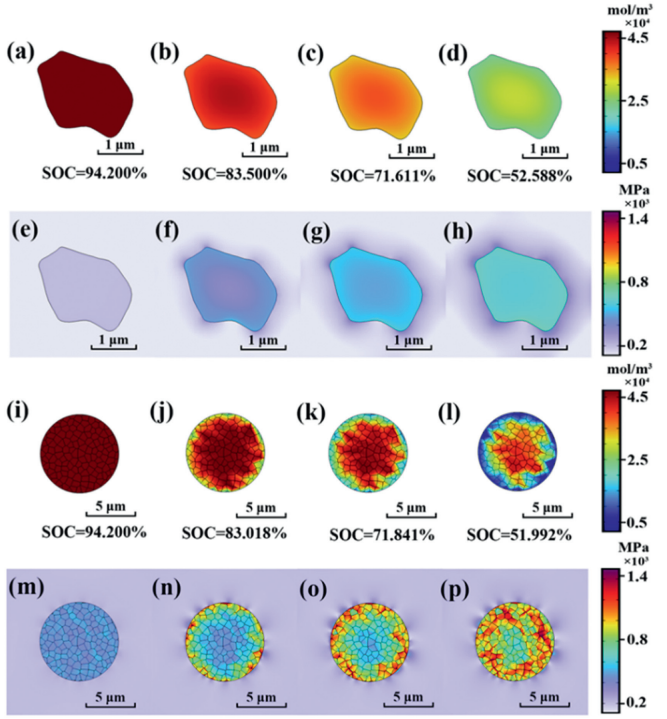


Fig. 5. COMSOL Simulation diagram of (a-d) charge distribution and (e-h) stress distribution during the charging process on the cathode surface of S-NCM83. Diagram of (i-l) charge distribution and (m-p) stress distribution during the charging process on the cathode surface of P-NCM83.

Bode plot curve also reaches its maximum, suggesting that the interfacial impedance of the battery is affected by the material phase transition process during charging. Subsequently, during the discharge process, the semicircle in the low-frequency region of the Nyquist plot becomes smaller, and the amplitude of the Bode plot curve decreases accordingly. Furthermore, the Nyquist plots and Bode plots of S-NCM83 battery during the first charging process were shown in Figs. 3c and d, respectively. Compared to P-NCM83, the amplitudes of the Nyquist plot and Bode plot curves of the S-NCM83 battery exhibit smaller changes during both charging and discharging, indicating a more stable interfacial impedance.

Furthermore, we quantified the resistance during the first two cycles of charging/discharging process for the NCM batteries to evaluate the evolution of interfacial impedance (Figs. S7 and S8 in Supporting information). To adequately fit the Nyquist plots, an equivalent circuit model incorporating four resistances was employed (Fig. S9 in Supporting information) [45]. Specifically, the resistance R_0, intercepting the real axis at high frequencies, represents the intrinsic ohmic resistance. The semicircle at high frequencies corresponds to the bulk resistance of the solid-state electrolyte (R_{SE}). Meanwhile, the semicircles at medium and low frequencies signify the cathode/electrolyte interface resistance (R_{ct1}) and anode/electrolyte interface resistance (R_{ct2}), respectively.

As shown in Fig. 4a, the ohmic resistance (R_0) and the electrolyte resistance RSE remain relatively stable at 25 Ω and 18 Ω, respectively, during the charging and discharging processes. In contrast, R_{ct1} and R_{ct2} exhibit significant fluctuations and clear periodic variations during these cycles. During the first charging process, R_{ct2} in the P-NCM83 battery rapidly increases with rising voltage. During discharging process, as the voltage decreases to 3.0 V, lithium ions extract from the lithium-indium anode, resulting in a lower lithium-ion concentration in the anode and a significantly increase of R_{ct2}. However, upon the second charging, R_{ct2} swiftly decreases back to 30 Ω and remains stable during subsequent charging.

Apart from the anode side resistance (R_{ct2}), during the charging process, the cathode side interface resistance (R_{ct2}) of the P-NCM83 battery delivers a significant increase. Especially during H2-H3 phase transitions (OCV > 3.5 V), R_{ct2} have an increase by approximately 210 Ω, indicating to the poor ion transport kinetics during the phase transitions process. During discharge, as the voltage decreases, the resistance promptly diminishes. Notably, R_{ct2} after the second charging process and second discharging process is higher for approximately 71 and 28 Ω, respectively, than that of in first cycle, indicating a higher a higher interfacial kinetic resistance, which is primarily associated with irreversible phase transitions and side reactions of P-NCM83 cathode. During the long-term cycling process, the sluggish interfacial kinetic resistance can induce a heterogeneous ion transport and charge distribution in active secondary particle.

Additionally, the impedance evolution of the S-NCM83 battery are presented in Fig. 4b. R_{ct2} exhibits similar values and trends as those observed in the S-NCM83 battery. However, there is a significant difference in R_{ct1}. During the initial charging process, R_{ct1} only increases by 55 Ω, indicating a faster kinetic during the delithium process. Compared to the first cycle, the resistance after the second charging of the S-NCM83 battery is merely 55 Ω higher, and the resistance during the second discharge is approximately 23 Ω higher than that of the first discharge, suggesting fewer irreversible reactions. Importantly, R_{ct2} increase after the second charging process and second discharging process is approximately 55 and 23 Ω, respectively, which is lower than that of in P-NCM83, indicating a fewer irreversible phase transition and phase reactions during the charging-discharging process of S-NCM83. The relatively small and stable interfacial resistance of S-NCM83 enables the active particles to maintain rapid and uniform charge transfer and reduce the performance degradation and structural failure.

To further explore the Li ion transport of NCM cathodes in sulfide-based ASSBs, COMSOL software was employed to simulate the charge distribution and stress distribution in S-NCM83 and P-NCM83 cathodes during the charging process. As depicted in Figs. 5a-d, due to the smaller particle size and fewer grain boundaries of single-crystal particles (S-NCM83), lithium ions can uniformly propagate along two-dimensional channels within the crystal lattice of single crystals, with shorter transport paths. During the charging process, the uniform ion transport direction in single-crystal particles results in a correspondingly homogeneous charge and stress distribution, which can mitigate structural degradation (Figs. 5e-h).

In contrast, larger polycrystalline particles are composed of randomly stacked primary particles, featuring numerous grain boundaries with random orientations. Therefore, in solid-state batteries with solid-solid ion transport, P-NCM83 exhibits longer ion transport paths and random transport directions. As shown in Figs. 5i-l, the charge distribution in P-NCM83 materials is uneven. In addition, the increase of interfacial ion transport resistance caused by the interfacial side reaction will induce nonequilibrium electrochemical reactions and further lead to the uneven charge of the P-NCM83 particle. This unequilibrated charge distribution readily leads to mismatched strain fields, resulting in stresses along grains and within grain interiors (Figs. 5m-p). Additionally, shear stresses along grain boundaries are imposed due to phase transitions during the charging process. Under the combined effects of resulting stress field, P-NCM83 materials are prone to forming intergranular cracks and induce a contact loss of cathode and electrolyte after extended cycling, restricting solid-solid ion transport and leading to performance degradation.

To verify the cycling stability of single-crystalline high-nickel cathode materials, morphology characterizations on both pristine and cycled electrodes were conducted and shown in Figs. S10-S12 (Supporting information). These results above confirmed the excellent structural stability of S-NCM83 cathode. Except for the structural stability, the chemical stability is important for single-crystalline high-nickel cathode materials in sulfide-based ASSBs. As shown in Fig. S13 (Supporting information) compared with cycled P-NCM83 electrode, S-NCM83 cathode delivers better chemical stability and less side reaction between LPSCl during the long cycling process.

In this work, we systematically explored the influence of crystal morphology on the electrochemical performance, interfacial ion transport and microstructure of Nickel-rich layered oxide cathode materials in sulfide-based ASSBs. From the electrochemical impedance spectroscopy and characterization results, polycrystalline P-NCM83 suffer from the heterogeneous localized environment and phase transition during the cycling process, which can easily lead to the formation of intergranular cracks, restricting solid-solid ion transport and causing performance degradation. While single-crystalline S-NCM83 cathode materials delivers a stable interfacial resistance and the uniform ion transport direction results in a correspondingly homogeneous charge and stress distribution, which can maintain a stable crystal structure and cycling stability. Therefore, compared with P-NCM83, the S-NCM83 cathode can deliver a higher specific capacity after 500 cycles at 0.5 C with a capacity retention rate of 89.2%, while maintaining an intact single-crystalline morphology. This work comprehensively investigates the effect of the crystal morphology of the ultrahigh-nickel cathode material for sulfide-based ASSBs, which will support the development of the ultrahigh-nickel NCM cathode materials.

Declaration of competing interests

The authors declare that they have no known competing financial interests or personal relationships that could have appeared to influence the work reported in this paper.

CRediT authorship contribution statement

Shanyan Huang: Writing – original draft, Conceptualization. **Bi Luo:** Writing – original draft, Investigation, Conceptualization. **Zixun Zhang:** Software, Methodology, Data curation. **Qi Wang:** Software, Resources, Methodology. **Guihui Yu:** Software, Resources, Formal analysis. **Xudong Bu:** Project administration, Methodology. **Zheng Huang:** Validation, Supervision, Project administration. **Xiaowei Wang:** Writing – review & editing, Validation, Funding acquisition. **Wei-Li Song:** Visualization, Validation, Supervision. **Jiafeng Zhang:** Writing – review & editing, Visualization, Funding acquisition. **Shuqiang Jiao:** Writing – review & editing, Project administration, Methodology, Conceptualization.

Acknowledgments

This work was financially supported by National Natural Science Foundation of China (No. 51902347) and Fundamental Research Funds for the Central Universities of Central South University (No. 2022ZZTS0439).

Supplementary materials

Supplementary material associated with this article can be found, in the online version, at doi:10.1016/j.cclet.2024.110729.

References

[1] J.W. Choi, D. Aurbach, Nat. Rev. Mater. 1 (2016) 16013.
[2] B. Aktekin, A.E. Sedykh, K. Müller-Buschbaum, et al., Adv. Funct. Mater. 34 (2024) 2313252.
[3] X. Ren, H. Liu, J. Wang, et al., Chin. Chem. Lett. 35 (2024) 109282.
[4] S. Chu, A. Majumdar, Nature 488 (2012) 294–303.
[5] B. Luo, Q. Wang, W. Ji, et al., Chem. Eng. J. 492 (2024) 152152.
[6] M.C. Liu, Q.S. Liu, Y.Z. Quan, et al., Chin. Chem. Lett. 35 (2024) 109123.
[7] T.T. Vu, H.J. Cheon, S.Y. Shin, et al., Energy Storage Mater. 61 (2023) 102876.
[8] B. Luo, W. Wang, Q. Wang, et al., Chem. Eng. J. 460 (2023) 141329.
[9] H. Zhang, Z. Yu, J. Cheng, et al., Chin. Chem. Lett. 34 (2023) 108228.
[10] Q. Liu, Q. Chen, Y. Tang, et al., Electrochem. Energy Rev. 6 (2023) 15.
[11] J. Janek, W.G. Zeier, Nat. Energy 8 (2023) 230–240.
[12] L. Ming, D. Liu, Q. Luo, et al., Chin. Chem. Lett. 35 (2024) 109387.
[13] C. Gao, J. Zhang, C. He, et al., Adv. Energy Mater. 13 (2023) 2204386.
[14] C. Wei, X. Liu, C. Yu, et al., Chin. Chem. Lett. 34 (2023) 107859.
[15] M.A. Kraft, S.P. Culver, M. Calderon, et al., J. Am. Chem. Soc. 139 (2017) 10909–10918.
[16] C. Fan, M.K. Tufail, C. Zeng, et al., ACS Appl. Mater. Interfaces 16 (2024) 28342–28352.
[17] J. Lau, R.H. DeBlock, D.M. Butts, et al., Adv. Energy Mater. 8 (2018) 1800933.
[18] X. Zhu, L. Wang, Z. Bai, et al., Nano-Micro Lett. 15 (2023) 75.
[19] B. He, F. Zhang, Y. Xin, et al., Nat. Rev. Chem. 7 (2023) 826–842.
[20] S.P. Culver, R. Koerver, W.G. Zeier, et al., Adv. Energy Mater. 9 (2019) 1900626.
[21] K.J. Kim, M. Balaish, M. Wadaguchi, et al., Adv. Energy Mater. 11 (2021) 2002689.
[22] D. Cao, Y. Zhao, X. Sun, et al., ACS Energy Lett 5 (2020) 3468–3489.
[23] W. Zhong, J. Tao, Y. Chen, et al., Adv. Pow. Mater. 3 (2024) 100184.
[24] Y. Park, J.H. Chang, G. Oh, et al., Small 20 (2024) e2305758.
[25] J.H. Wu, L. Shen, Z.H. Zhang, et al., Electrochem. Energy Rev. 4 (2021) 101–135.
[26] L. Li, H. Duan, J. Li, et al., Adv. Energy Mater. 11 (2021) 2003154.
[27] S. Wang, W. Zhang, X. Chen, et al., Adv. Energy Mater. 24 (2021) 2100654.
[28] B. Gao, R. Jalem, Y. Tateyama, ACS Appl. Mater. Interfaces 13 (2021) 11765–11773.
[29] H. Xu, Y. Su, C. Zheng, et al., Chin. Chem. Lett. 35 (2024) 109173.
[30] Y. Su, Q. Zhang, L. Chen, et al., J. Energy Chem. 65 (2022) 236–253.
[31] Y. Bi, J. Tao, Y. Wu, et al., Science 370 (2020) 1313–1317.
[32] P. Yan, J. Zheng, T. Chen, et al., Nat. Commun. 9 (2018) 2437.
[33] B. Luo, H. Li, H.Y. Qi, et al., J. Energy Chem. 88 (2024) 327–335.
[34] X. Zhang, Z. Wang, X. Li, et al., Mater. Horiz. 10 (2023) 1856.
[35] R. Tian, Z. Wang, J. Liao, et al., Adv. Energy Mater. 13 (2023) 2300850.
[36] C. Wang, S. Hwang, M. Jiang, et al., Adv. Energy Mater. 11 (2021) 2100210.
[37] X. Wang, M. Zhou, Y. Deng, et al., Chin. Chem. Lett. (2024) 110307.
[38] D. Shin, J.S. Nam, C.T. Linh Nguyen, et al., J. Mater. Chem. A 10 (2022) 23222–23231.
[39] X. Liu, B. Zheng, J. Zhao, et al., Adv. Energy Mater. 11 (2021) 2003583.
[40] W. Jiang, X. Fan, X. Zhu, et al., J. Power Sources 508 (2021) 230335.
[41] X. Zhou, F. Liu, Y. Wang, et al., Adv. Energy Mater. 12 (2022) 2202323.
[42] C. Wei, Y. Xiao, Z. Wu, et al., Sci. China Chem. 67 (2024) 1990–2001.
[43] X. Ou, T. Liu, W. Zhong, et al., Nat. Commun. 13 (2022) 2319.
[44] C. Wang, R. Zhang, K. Kisslinger, et al., Nano Lett. 21 (2021) 3657–3663.
[45] R. Koerver, I. Aygün, T. Leichtweiß, et al., Chem. Mater. 29 (2017) 5574–5582.